Applied Surface Science 585 (2022) 152744

Contents lists available at ScienceDirect

Applied Surface Science

journal homepage: www.elsevier.com/locate/apsusc

Full Length Article

Room-temperature gas sensors based on titanium dioxide quantum dots for highly sensitive and selective H_2S detection

Kaidi Wu [a,b], Wentao Zhang [a], Zichen Zheng [a], Marc Debliquy [b], Chao Zhang [a,*]

[a] College of Mechanical Engineering, Yangzhou University, Yangzhou 225127, PR China
[b] Service de Science des Matériaux, Faculté Polytechnique, Université de Mons, Mons 7000, Belgium

ARTICLE INFO

Keywords:
Quantum dots
Titanium dioxide
Gas sensor
Hydrogen sulfide
Room temperature

ABSTRACT

Room-temperature gas sensors with high performance are crucial in practical application. This work prepared a series of controllable-size titanium dioxide quantum dots (TiO_2 QDs) via a rapid microwave-assisted solvothermal method for detecting ppb-level H_2S at room temperature. The effect of reaction temperature on the nanostructure and gas sensing properties was investigated systematically. The characterization results showed the samples presented ultra-small size (around 5–6 nm) nanostructure and modified surface state (including Ti^{3+} and oxygen defects). The S120-TiO_2 QDs gas sensor showed the best sensing properties towards ppb-level H_2S at room temperature, including high response (25.12 @ 500 ppb H_2S), rapid response/recovery, low detecting limit level, good selectivity, and operating stability. The gas sensing mechanism was explained through the synergetic effect of ultra-small size nanostructure, large specific surface area, and surface defects, which are in favor of improving the surface activity and charge transfer efficiency. Moreover, the practical application of TiO_2 QDs gas sensor in detecting the volatiles of fish (Pangasius) was also verified. This work developed a room temperature TiO_2 quantum dots-based gas sensor, which is promised for practical application because of the rapid synthesis and high performance.

1. Introduction

Hydrogen sulfide (H_2S) is a kind of malodorous and toxic gas. Once people are exposed to H_2S for a long time, it will present a serious threat to human central nervous and respiratory symptoms [1]. Though the olfactory threshold of the human nose for hydrogen sulfide is 130 ppb, continuous exposure will cause a sharp decline in the ability to smell and even paralysis [2]. Hence, the safety concentration of H_2S for human health conditions is recommended not to exceed 100 ppb [3]. In addition, H_2S is also a component of poultry meat or fish freshness biomarker gas released via microorganisms and endogenous enzymes decomposing sulfhydryl-containing amino acids and proteins [4]. The concentration of released H_2S will reach or even exceed ppb level if the meat starts to deteriorate [5]. Furthermore, the variation of trace-amounts H_2S in human exhaled breath is recommended as a biomarker to diagnose some diseases, including halitosis and periodontal disease [6]. Hence, there is an urgent need for a rapid and precise detection technique towards low-concentration H_2S.

A series of metal oxide-based gas sensing sensors with the low-cost and easy operation have been developed, such as WO_3[7], CuO [8], Co_3O_4[9], and TiO_2[10]. Among them, TiO_2 (~3.2 eV) belongs to the wide-bandgap semiconductor, which has been studied as a promising gas sensing materials own to its excellent electron mobility and chemical stability [11]. Alenezy et al. developed light-activated H_2 sensors based on Pd-TiO_2 crystals using a multi-step process, showing a low operating temperature but poor response [12]. Galstyan et al. fabricated two kinds of TiO_2 based gas sensors (Nb-TiO_2 and Nb-TiO_2-rGO). The sensors showed a good sensitivity to H_2 at 200 °C [13]; Šutka et al. synthesized anatase TiO_2 quantum dots, and the gas sensors presented similar responses to various volatile organic compounds (VOCs) under UV illumination [14]. Therefore, TiO_2 based gas sensors still face the challenge of insufficient sensing properties at room temperature. Although several strengthened strategies have been proposed to improve sensitivity and selectivity, the high working temperature, insufficient detection limit and long recovery time remain [15–17]. Especially, the high working temperature will lead to the growth of grain size and higher power consumption. Lowering the working temperature can also simplify the fabrication of the sensors and enhance the stability of the sensing materials. Hence, it has become a significant research objective to lower the operating temperature of semiconductor gas sensors to room

* Corresponding author at: College of Mechanical Engineering, Yangzhou University, Huayang West Road 196, Yangzhou 225127, Jiangsu Province, PR China.
E-mail address: zhangc@yzu.edu.cn (C. Zhang).

https://doi.org/10.1016/j.apsusc.2022.152744
Received 19 December 2021; Received in revised form 26 January 2022; Accepted 3 February 2022
Available online 10 February 2022

temperature. As for this demand, Wu et al. synthesized ellipsoids-like α-Fe_2O_3 nanomaterials and the corresponding gas sensor showed fast response/recovery and fine selectivity to ppb level H_2S [18]. Liu et al. developed SnO_2 colloidal quantum dots based H_2S sensor working at low temperature utilizing the benefits of ultra-small grain size effect and high surface activity [19]. Therefore, novel nanostructure has been considered as an effective pathway for lowering gas molecules' adsorption/desorption energy and improving electron transfer efficiency to achieve promised room-temperature gas sensing properties [20–22].

Herein, we utilized a rapid microwave-assisted solvothermal method to prepare anatase TiO_2 quantum dots and fabricated high-performance room temperature H_2S sensors. The effect of reaction temperature on grains size and sensing properties was investigated. The as-fabricated room temperature TiO_2 QDs gas sensor achieved high sensitivity, rapid response/recovery speed, sufficient limit of detection, selectivity, and operating stability towards ppb-level H_2S. The excellent sensing properties were explained by the synergistic effects of the quantum size effect (superior surface activity to target gas), surface defects, and the large specific surface area (providing abundant sites for gas molecules adsorption). Furthermore, the application of S120 gas sensor in detecting the volatiles of fish (Pangasius) was also investigated to verify its practical potential.

2. Experimental section

2.1. Synthesis of TiO_2 quantum dots

All reagents were used without further purification (Sinopharm Chemical Reagent Co., Ltd.). TiO_2 quantum dots were synthesized via as following procedures: 30 mL absolute ethanol and 3 mL nitric acid aqueous solution (3 M) was mixed in a beaker and stirred for 30 min. Subsequently, 10 mL tetrabutyl titanate (TBT), was dropped into the above solution slowly. After magnetically stirring for 1.5 h, it was transferred to a 60 mL Teflon autoclave and placed into the microwave solvothermal synthesis instrument (XH-800G, Beijing Xianghu Technologies Development Co., Ltd.). It was then maintained at 120 °C and 500 W for 1 h and cooled down naturally. The obtained precipitation was centrifuged (5000 rpm, 10 min) 4 times with absolute ethanol and eventually dried at 60 °C for 10 h. The other samples were obtained through only changed reaction temperatures as 90 °C, 150 °C and 180 °C. The three samples are denoted as S90, S120, S150, and S180.

2.2. Characterization

The crystal structure of all samples was identified using X-ray diffraction with Cu-Kα radiation (XRD, D8 Advance Bruker). Ultraviolet–visible (Uv–vis) absorption ability was determined via a Uv–vis diffuse reflectance spectrophotometer (Cary5000, Varian, USA). The morphology of TiO_2 was inspected using field-emission scanning electron microscopy (FESEM, S4800II Hitachi). The nanostructure was determined via transmission electron microscopy (TEM, JEM-2100), and further analysis was conducted using high-resolution transmission electron microscopy (HRTEM, Tecnai G2 F30 S-TWIN). X-ray photoelectron spectroscopy (XPS, Thermo Fisher Scientific ESCALAB 250Xi) was used to analyze surface chemical compositions. The specific surface area was calculated through N_2 adsorption/desorption isotherms at 77 K (Autosorb IQ3, Quantachrome Instruments).

2.3. Fabrication and tests of gas sensors

The as-prepared powder was directly used to obtain its slurry with deionized water, subsequently coated onto the sensor substrate. The gas sensor was obtained after dried and treated at 120 °C for 24 h. Fig. S1 shows the gas sensing testing, and the sensor measurement steps are shown in supporting information. Furthermore, the response of n-type TiO_2 is defined as R_a/R_g, where R_a is the stable sensor resistance and R_g is the stable sensor resistance is in target gas to the stable resistance in air. The response/recovery time is the time taken for achieving 90% change of resistance in the response and recovery behaviors.

The fish spoilage detection is explored through homemade measurement equipment (Fig. S2). 25 g fresh Pangasius fillet was placed in a 0.6 L sealed bottle at room temperature, and the variation of electrical resistance at different storage stages (1, 6, 12, 18 and 24 h) was recorded.

3. Results and discussion

3.1. Material synthesis and structural properties

The phase compositions of four powders are shown in Fig. 1a. S90 showed a series of weak peaks, indicating there is not a good crystallinity, so its theory grain size was not calculated. As for the other three powders, these distinct diffraction peaks observed from 20° to 80° are well indexed to anatase TiO_2 with the tetragonal crystal structure (JCPDS cards No. 21–1272), the corresponding lattice constants are a = b = 3.785 Å, c = 9.514 Å and α = β = γ = 90°. There are no extra peaks, implying the obtained TiO_2 possessed perfect phase structure and high purity, even it was synthesized at a lower solvothermal temperature. In addition, Fig. 1b showed the XRD patterns from 22° to 30° were also tested in a slow scan speed of $2^o \cdot min^{-1}$. With the increasing reaction temperature, the peak positions of TiO_2 have a slight shift to low angle, narrower width, and stronger intensity. It indicates that the grain size in S150 and S180 increases, resulting from the higher temperature of crystal nucleation and grain growth temperature. Furthermore, the average grain sizes of anatase TiO_2 were then confirmed using the Debye-Scherrer equation:

$$D = 0.89\lambda/\beta\cos\theta \quad (1)$$

where λ is the wavelength of the Cu K α radiation ($\lambda = 0.15418$ nm), β is the peak width at half maximum (FWHM) of anatase TiO_2 planes, and θ is the position of XRD peaks. As shown in Table S1, the crystal sizes were 5.0 nm, 5.6 nm, and 6.0 nm, respectively.

FESEM images of as-synthesized samples are displayed in Fig. S3. The ultra-small nanoparticles showed good dispersion and less agglomeration. With increasing the reaction temperature, the agglomerations of S150 and S180 occurred obviously. The nanostructures of all samples were further analyzed through TEM. The nanostructures of all samples were further analyzed through TEM. In Fig. S4, S90 TiO_2 agglomerated into a cluster, and due to the crystallinity of TiO_2 being too poor, no obvious TiO_2 particles can be seen. And even part of TiO_2 does not form crystal grains and exists in the amorphous state. In Fig. 2, the TiO_2 (S120) prepared under a solvothermal temperature of 120 °C showed uniformly distributed quantum dots, while S150 and S180 samples showed the larger nanoclusters composed with amounts of quantum dots. Based on the images and XRD results, the higher temperature not only improved the crystalline of TiO_2 but also was in favor of grain growth. Additionally, the agglomeration of TiO_2 grains occurred at the elevated reaction temperature. As shown in Fig. 2d, the grain sizes of S120 were measured from 100 particles, which obey the normal distribution, and the average size was 5.6 nm. The small sizes effect will contribute to enhancing gas sensing properties, which is further described in the gas sensing mechanism. The HRTEM image of S120 (Fig. 2e) further confirms the presence of anatase phase with the crystalline interplanar spacing of 0.356 nm indexed to the (1 0 1) plane of TiO_2 quantum dots. Furthermore, the uniform element distribution of Ti and O in S120 powder was displayed in Fig. 2f. According to the characterization results, the synthesis mechanism of TiO_2 quantum dots is proposed in Fig. 2g. First, absolute ethanol and 3 M aqueous nitric acid were mixed to form an acid solvent system. Due to the ratio of Ti^{4+} to H_2O being low to 5.56 and the acidic condition, the percussor solution

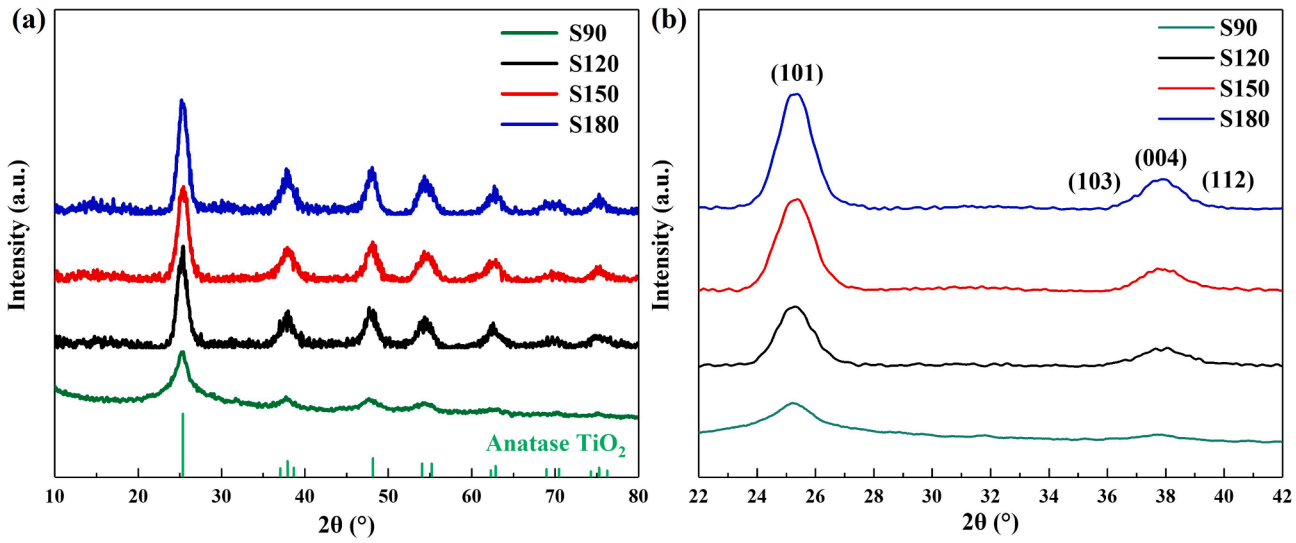

Fig. 1. XRD patterns of as-synthesized TiO_2 samples with the scan speed of (a) $5^{o}{\cdot}min^{-1}$ and (b) $2^{o}{\cdot}min^{-1}$.

was prepared via controlled hydrolysis TBT (A) [23]. Then anatase TiO_2 precipitations were generated under homogeneous microwave dielectric heating, which provided a uniform nucleation and growth environment (B) [24].

The energy bandgap of all the samples was estimated using UV–Vis absorption spectroscopy in the wavelength range from 200 nm to 800 nm. Fig. 3a showed a similar absorbance intensity in the UV range of all the samples. When the reaction temperature was increased, the corresponding absorbance intensity in the visible light range became stronger. As shown in Fig. 3b, the bandgap values of TiO_2 powders were estimated using the Tauc plots. The bandgap energies (E_g) of S90 (3.25 eV), S120 (3.22 eV), S150 (3.18 eV), and S180 (3.14 eV) decreased while the grains size increased in the range of quantum size. The results could be explained via the size quantization effect. The traps will shift to the higher energy side once grain size decreases below its critical size corresponding to the bandgap minimum, resulting in higher bandgap energy [25–27].

The element's chemical states of anatase TiO_2 quantum dots were determined through XPS. In Fig. 3c, the full survey spectrum revealed Ti and O existed in the as-synthesized powders. Fig. 3d displayed the high-resolution Ti 2p spectra with five fitted peaks. The peaks at 458.38 and 464.18 eV can be indexed to Ti^{4+} 2p3/2 and Ti^{4+} 2p1/2, respectively [28]. Meanwhile, the 457.93 and 462.83 eV peaks correspond to Ti^{3+} characteristically doublet peaks, respectively [29]. The distance of ~ 5.56 eV for S120 between the peaks at the binding energy of approximately 458.15 and 463.51 eV demonstrated the existence of both Ti^{3+} and Ti^{4+} in the powder [30]. Fig. 3e presents the O 1 s spectra of anatase TiO_2 quantum dots, which can be indexed to three peaks: lattice oxygen (O_L) at 529.48 eV, oxygen vacancies (O_V) at 530.83 eV, and surface adsorbed oxygen species (O_C) at 532.38 eV [31,32]. The chemical state composition will be in favor of the enhancement of gas sensing properties [33].

The BET-specific surface area of S120 TiO_2 quantum dots was tested and the isotherm plots of S120 TiO_2 are displayed in Fig. 3f. The specific surface area of S120 TiO_2 is 213.225 $m^2{\cdot}g^{-1}$. The nanostructure with a large surface area will contribute to improving gas molecules' adsorption and reaction, thus resulting in enhancing the sensing performance.

3.2. Gas sensing performance

The measurement of TiO_2 quantum dots-based gas sensors was carried out at room temperature. In Fig. 4a, the resistance variation to 500 ppb H_2S was obtained at the same test conditions. S90 with the lower crystallinity showed the highest baseline resistance (R_a) and the lowest response (R_a/R_g), while S120 showed the highest response. The effect of crystallinity and specific surface area on baseline resistance and response was discussed in "Gas sensing mechanism" section. S90 showed a relatively poor response, which may be caused by the weak crystallinity of the S90 sample. And the S120 gas sensor showed the highest response. Then, the role of the operating temperature of TiO_2 quantum dots-based gas sensors was investigated by exposing the sensors to 200 ppb H_2S. Fig. S5 showed the response-recovery curves of S120 TiO_2 quantum dots towards 200 ppb H_2S at 25–100 °C. The response values towards 200 ppb H_2S at various temperatures from 25 °C to 100 °C decreased from 4.75 to 3.25, indicating room temperature was the optimum operating temperature. The effect of sensing layer thickness on gas sensing properties was also investigated. Taking the S120 gas sensor as an example, we prepared a series of uniformed sensing films with 1–3 layers. The surface morphology of S120 sensing material layer on electrodes, the cross-section morphology and the thickness of different layers were studied using FESEM images. Fig. S6a shows the uniform distribution of S120 sensing material with 2 layers on the electrodes, which can ensure valid and stable gas sensing behavior. The thickness of S120 with different layers was also identified by cross-section FESEM observation. As shown in Fig. S6b-d, the thickness of sensing materials with 1, 2 and 3 layers are 10.78 μm, 12.38 μm and 20.60 μm, respectively. The sensing results showed that the thickness does affect the sensor response (Fig. S7). As the film thickness increases, the response decreases. As a result, one layer is currently the optimal thickness for our study.

Then, the effect of reaction temperature on TiO_2 quantum dots-based gas sensors was investigated via exposing the sensors to H_2S of various concentrations. Fig. 4b depicted the reversible response-recovery curves of TiO_2 quantum dots. All gas sensors showed fine responses to 100–500 ppb H_2S at room temperature, which could be ascribed to the small grains size effect [34]. The detail will be explained in the gas sensing mechanism. Notably, the response values of the S120 sensor were much higher than that of S150 and S180. Fig. 4c showed the corresponding responses of all sensors, the responses of S120 to 100–500 ppb H_2S were from 2.43 to 25.12, respectively, while those of S90, S150 and S180 were 1.5–11.35. The results indicate that the TiO_2 quantum dots sensor (S120) had a higher sensitivity for ppb level H_2S gas detection. Hence, we chose the S120 gas sensor for the rest of the test. From Fig. 4d, we found that the S120 gas sensor possessed an exponential relationship ($R^2 = 0.9994$) with H_2S concentration from 100 to 500 ppb via fitting the above data, which are in favor of the quantitative analysis [35,36].

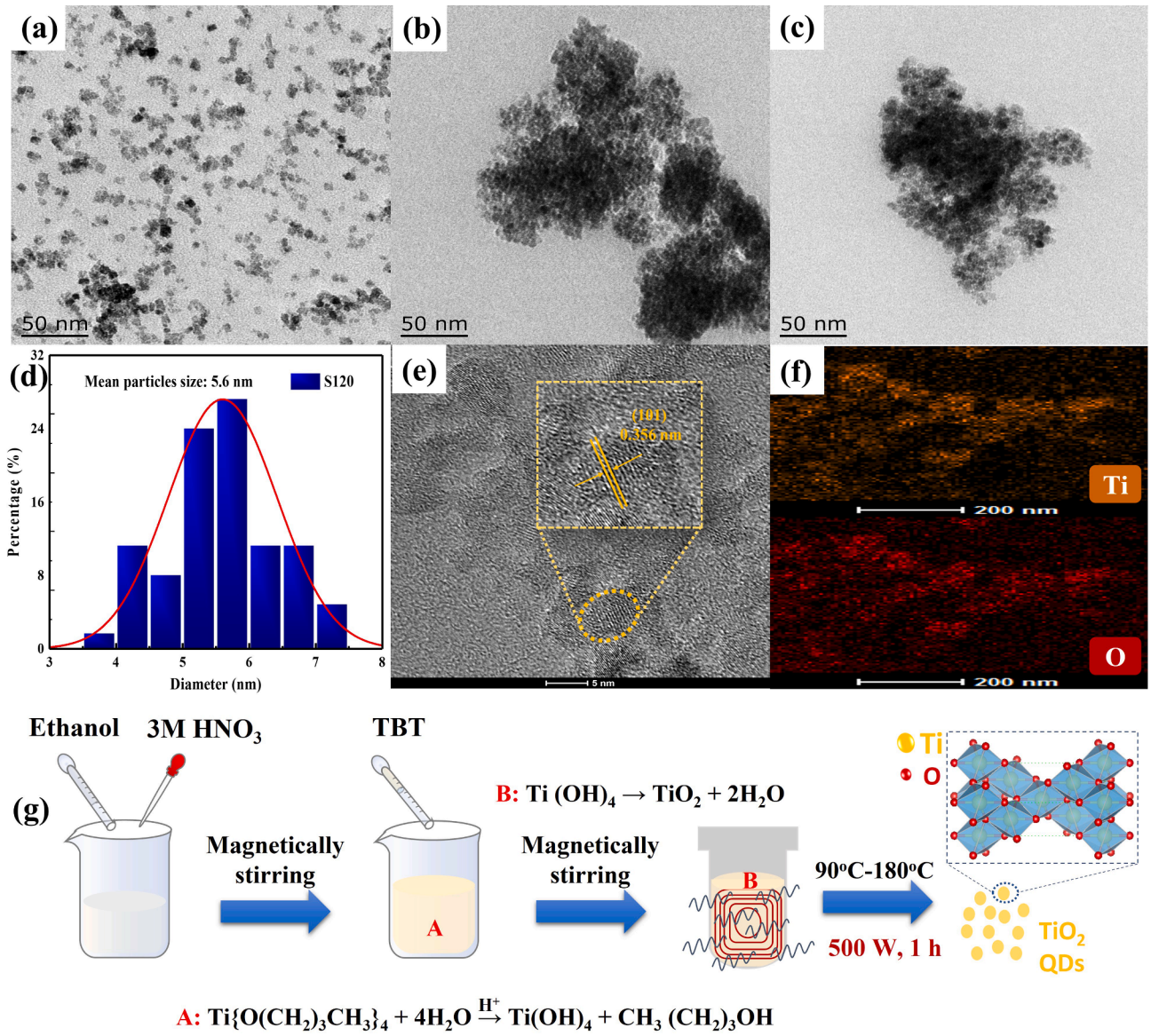

Fig. 2. TEM images of (a) S120, (b) S150 and (c) S180. (d) the distribution of particles size of S120. (e) HR-TEM image of S120. (f) EDS elements mappings of S120 sample. (g) The synthesis procedure and mechanism of TiO_2 samples.

Furthermore, the response/recovery speed of S120 was also measured at the same conditions. Fig. 4e showed the S120 gas sensor exhibited a fast response speed (34 s) to 500 ppb H_2S, while the recovery time was 470 s.

The selectivity of S120 gas sensor was also be tested using five interference gases of 500 ppb, including NH_3, SO_2, H_2, CH_3OH, C_8H_{10}, and C_2H_5OH. In Fig. 4f, the highest response value was 25.12 towards H_2S, while the responses to NH_3, SO_2, H_2, CH_3OH, C_8H_{10}, and C_2H_5OH were 1.11, 1.08, 1.06, 1.04, 1.02, and 1.01, respectively. The excellent selectivity of S120 gas sensor could be ascribed to the two aspects. First, it was reported that good selectivity could be attributed to the bond dissociation energies of the various target gases. H_2S (376 kJ·mol^{-1}) was smaller than that of ammonia (452 kJ·mol^{-1}), sulfide dioxide (523 kJ·mol^{-1}), hydrogen (436 kJ·mol^{-1}), methanol (461 kJ·mol^{-1}), toluene (389 kJ·mol^{-1}) and ethanol (462 kJ·mol^{-1}) [37]. Hence, H_2S will easily interact with chemisorbed oxygen species [38]. Additionally, the quantum-size TiO_2 will provide amounts of adsorbed sites for target gases, which will contribute to promoting the reaction between H_2S and surface chemisorbed oxygen species at the optimum operating temperature [39].

The effect of relative humidity on gas sensing performance was also tested. Fig. 4g showed the real-time response curves to 200 ppb H_2S at room temperature and various relative humidity. The responses of the gas sensor under different RH values (30, 40, and 50%) were 4.95, 3.52, and 2.52, respectively and the corresponding baseline resistance were 1 $\times$ 10^{10} Ω, 6.88 $\times$ 10^{9} Ω, and 4.06 $\times$ 10^{9} Ω, respectively. In Fig. S8, it can be found that both the response and the baseline resistance of S120 were decreased with an increase of relative humidity, which was attributed to that water molecules are adsorbed on the surface of the S120 sensor in the molecular or hydroxyl forms [40]. Repeatability and stability are the key roles of the gas sensor. In Fig. 4h, we tested the response cycles to 300 ppb H_2S at room temperature, and the response values were around 6.65. Fig. 4i showed the stable characteristics of the S120 gas sensor to 300 ppb H_2S in a week. The variation of response values towards 300 ppb H_2S did not exceed 3%, indicating that the TiO_2 quantum dots gas sensor attained a stable response at room temperature.

The comparisons of H_2S sensing properties between reported gas sensors and S120 gas sensors are summarized in Table 1. The S120 gas sensor presents superior room temperature H_2S sensing properties than other TiO_2 based gas sensors. Furthermore, compared with other reported semiconductors gas sensors, the S120 gas sensor still exhibits

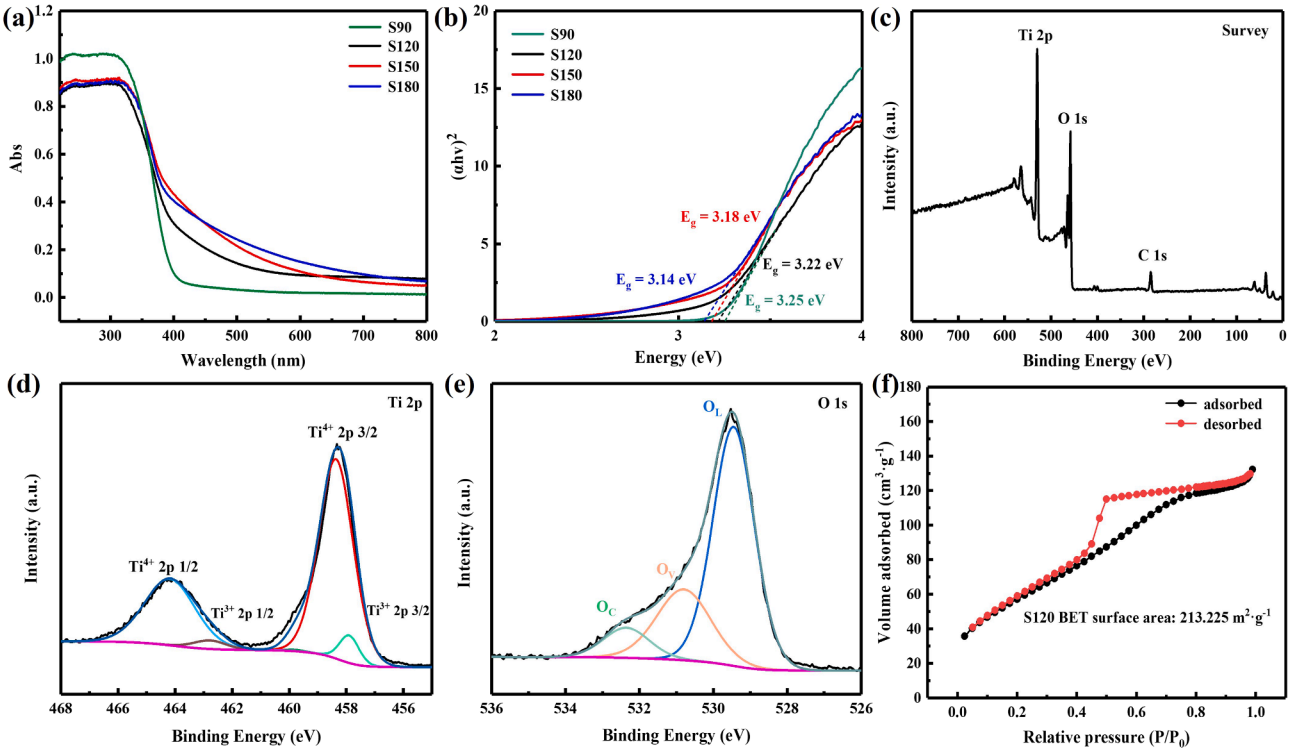

Fig. 3. (a) UV–Vis spectra. (b) Tauc plots of as-synthesized TiO_2 samples. Elements chemical states of anatase TiO_2 quantum dots determined via XPS: (c) survey, (d) Ti 2p and (e) O 1 s. (f) Nitrogen adsorption–desorption measurement isotherm of S120 sample.

advanced H_2S sensing properties.

3.3. Gas sensing mechanism

Fig. S9 shows there existed the augmented optical band gap in TiO_2 QDs due to the quantum confinement effect. Additionally, the TiO_2 QDs gas sensor underwent a considerable decrease in sensor resistance, resulting in a higher response to H_2S. Based on the characterization and testing results, the sensing mechanism of TiO_2 QDs was proposed based on the electron depletion region model and grain size effect.

According to the experimental results, we proposed a more detailed mechanism of the TiO_2 QDs gas sensor. In the view of transducer function, according to the comparison of grains size (D) with the Debye length (L), it can be clarified three models as grain boundaries control (D $\gg$ 2 L), neck control (D $\geq$ 2 L) and grains control (D < 2 L) [34,48]. The Debye length (L) is dependent on temperature (T) and carriers' concentration (e) as the following Eq. (2) [49,50]:

$$L = \sqrt{\frac{\varepsilon_0 \varepsilon_r kT}{e^2 N_D}} \quad (2)$$

where the permittivity of vacuum (ε_0) is around $8.8 \times 10^{-12} F \cdot m^{-1}$, the dielectric constant (ε_r) of anatase TiO_2 is 18.9, k is Boltzmann's constant (1.38×10^{-23} J/K), T is the absolute temperature (298 K), e is the charge of an electron (1.6×10^{-19}C), and N_D is the electron concentration. According to the reported carrier concentration of TiO_2 (10^{22}-10^{26} m^{-3}) [51,52], and since the tested TiO_2 was quite resistive, it is reasonable to assume that the charge carrier concentration is 10^{22} m^{-3}. The Debye length of TiO_2 QDs at room temperature can be estimated as around 50 nm, which is consistent with the results (10–100 nm) in reported literature [51]. The estimated average grain size from XRD and TEM was about 5 nm, which is much smaller than the twice Debye length. Under this condition, fully depleted regions are highly probable.

Fig. 5a displays the schematic response procedure of the fabricated TiO_2 QDs based H_2S sensor on the alumina substrate. When sensors are exposed to air, oxygen molecules ($O_{2\ (gas)}$) will be adsorbed on the surface of the material to form adsorbed oxygen molecules ($O_{2\ (ads)}$) that will capture electrons from the surface and generate oxygen ions (Eq. 3 and 4). Once sensors are exposed to H_2S, the chemical reaction between oxygen ions with H_2S molecules (Eq. 5 and 6) will release electrons. There will present a complete depletion region in ultra-small size TiO_2 QDs sensing materials. The grain control model is conducive to showing a remarkably high gas sensitivity [53]. As shown in Fig. 5b, after the electrons were all captured from the whole grain, the flat energy band without charge transfer barriers would be formed at interfaces. Meanwhile, there will generate a low conductivity. Once exposed to H_2S gas, the electrons will be released back and the whole nanograins gain a high conductivity.

$O_{2\ (gas)} \rightarrow O_{2\ (ads)}$(3)

$O_{2\ (ads)} + e^- \rightarrow O_2^-{}_{(ads)}$ (RT)(4)

$H_2S_{\ (gas)} \rightarrow H_2S_{\ (ads)}$(5)

$2H_2S_{\ (ads)} + 3O_2^-{}_{(ads)} \rightarrow 2SO_2 + 2H_2O + 3e^-$ (RT)(6)

Based on the complete depletion model, it is proposed to calculate the sensing response via Eq. 7–9 (setting the electron mobility (μ) as a constant; σ_a and σ_g is the electrical conductivity in air and gas, respectively) [53]:

$$S = R_a/R_g = \sigma_g/\sigma_a \quad (7)$$

$$\sigma_a \approx \exp(-\frac{E_{Ca} - E_F}{k_0 T}) \quad (8)$$

$$\sigma_g \approx \exp(-\frac{E_{Cg} - E_F}{k_0 T}) \quad (9)$$

where T is the working temperature of the sensor (absolute temperature). The final calculation could be written as $S = \exp(\frac{E_{Ca} - E_{Cg}}{k_0 T})$, which is consistent with the fitting curve of experimental data (Fig. 4d).

As for the enhanced mechanism of S120, it could be explained based on high crystallinity, specific surface area and surface defects. First, it is

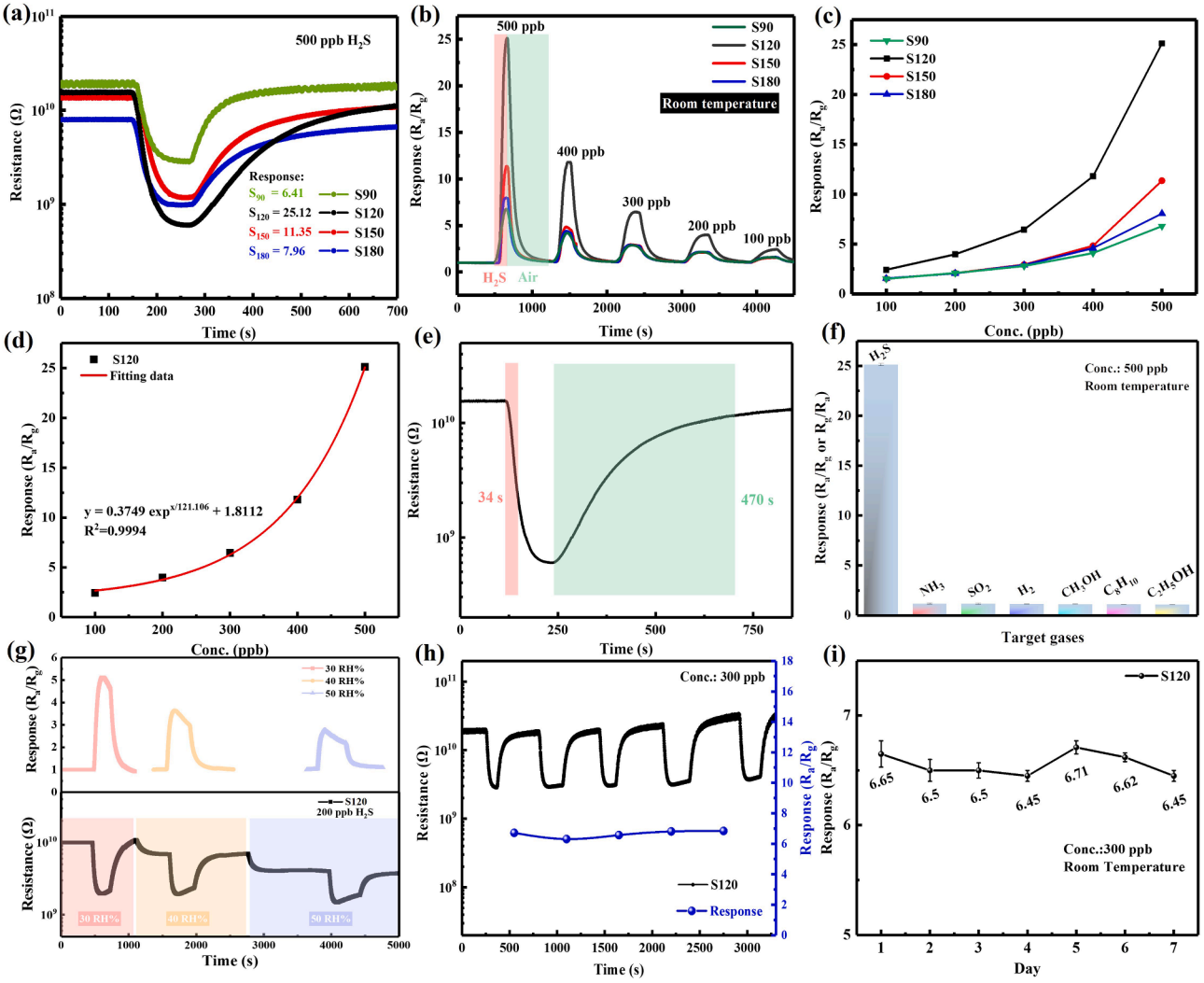

Fig. 4. (a) Resistance variation of four gas sensors to 500 ppb H_2S at room temperature. (b) Dynamic response/recovery curves of four samples to 100–500 ppb H_2S at room temperature. (c) Responses values to 100–500 ppb H_2S at room temperature. (d) Relationship of responses values versus H_2S concentration. (e) Responses /recovery time of S120 to 500 ppb H_2S at room temperature. (f) Selectivity to 500 ppb H_2S and various gases of S120 at RT. (g) real-time response to 200 ppb H_2S of S120 at different relative humidity. (h) Response to 300 ppb H_2S of S120 in 5 cycles. (i) Response stable characteristics of S120 sensor to 300 ppb H_2S in a week.

Table 1
Comparison of H_2S sensing properties for different metal oxides semiconductor sensors.

Materials	Preparation methods	Working Condition	Conc.	Response (R_a/R_g)	Refs.
TiO_2 Nanoparticulate	Bar coating	UV & RT	5000 ppb	4.2	[41]
TiO_2 nanotubes	Anodization	300 °C	1000 ppb	4.5	[42]
Fe-TiO_2 nanotubes	Anodization	100 °C	1000 ppb	2.0	[43]
Ag-TiO_2 nanofibers	Electrospinning	350 °C	500 ppb	1.4	[44]
α-Fe_2O_3 nanoparticles	Hydrothermal & post-thermal annealing	200 °C	1000 ppb	7.9	[45]
In_2O_3 QDs	Solvothermal	Near RT	1000 ppb	1.2	[46]
Ag-MoO_3 nanobelts	Hydrothermal	133 °C	1000 ppb	6.4	[47]
TiO_2 QDs (S120)	Microwave-assisted solvothermal	RT	500 ppb	25.12	This work

known that the carrier concentration and mobility of a nanomaterial could be influenced by its crystallinity [54]. Lower crystallinity of sensing materials may lead to a higher resistivity, and a decreased response when exposed to target gases [55]. Hence, S90 showed the worst sensing performance. Second, the synthesized S120 TiO_2 showed a large specific surface area of 213.225 $m^2 \cdot g^{-1}$, which is feasible to provide abundant reactive sites and attain better sensing performance. According to the reported literature, the specific surface area is related to grain size (A = 6 / D * ρ, where A is the specific surface area, D is the grain size, and ρ is the density of the crystal), suggesting that specific surface area will decrease with increasing grain size [56]. Therefore, S120 showed superior sensing properties than S150 and S180 TiO_2 with larger grain size. Besides, the XPS results of Ti 2p and O 1 s in as-synthesized S120 TiO_2 proved that there existed Ti^{3+} and oxygen defects on the surface, which was in favor of providing abundant sites for the gases molecules adsorption and improving gas sensing properties

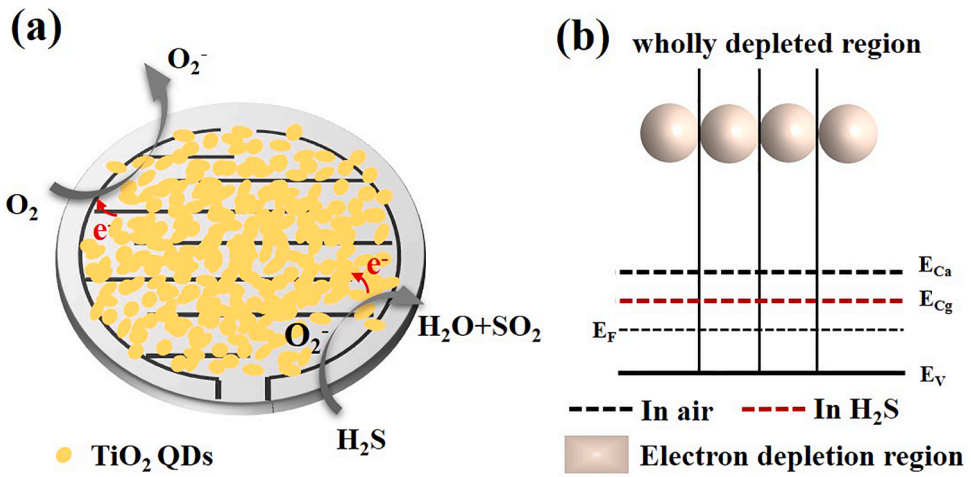

Fig. 5. (a) Schematic diagram of TiO_2 QDs gas sensor for detecting H_2S. (b) wholly depleted region and "flat-band" model for grains size with D < 2 L.

[32,57].

3.4. Fish spoilage detection

The practical application of the proposed gas sensor should be investigated to evaluate the application potential. Due to the decomposition of sulfhydryl-containing amino acids, there will release gases during the fish spoilage process [58]. Herein, the practicability of our sensor to detect fish (Pangasius) freshness was studied. As shown in Fig. S2, it was used to detect the H_2S released from 25 g fish during the storage at room temperature. In Fig. 6a-e, the response of the S120 gas sensor increased from 1.24 to 2.01, along the storage time became longer. As shown in Fig. 6f, the S120 gas sensor showed increased response values to the released gas. Additionally, the photographs also presented the color of fish became darker during the storage, indicating the beginning of fish deterioration. Hence, the results further confirmed the practical potential of the S120 gas sensor for H_2S detection.

4. Conclusions

Anatase TiO_2 quantum dots gas sensors were fabricated through a microwave-assisted solvothermal technique and coating method. The powders with different grains sizes were obtained via adjusting the reaction temperature as 90 °C, 120 °C, 150 °C, and 180 °C. The S120 sample showed a quantum dots nanostructure with good crystallinity and a small grain size of around 5 nm. The S120 gas sensor showed the highest response of 2.43–25.12 to 100–500 ppb level H_2S at room temperature and around 30 %RH, as well as improved detecting limit level, selectivity, and operating stability. The excellent gas sensing properties were ascribed to the synergetic effect of the ultra-small size, large specific surface area, and surface defects. Moreover, the practical application of S120 gas sensor in detecting the fish (Pangasius) spoilage was explored.

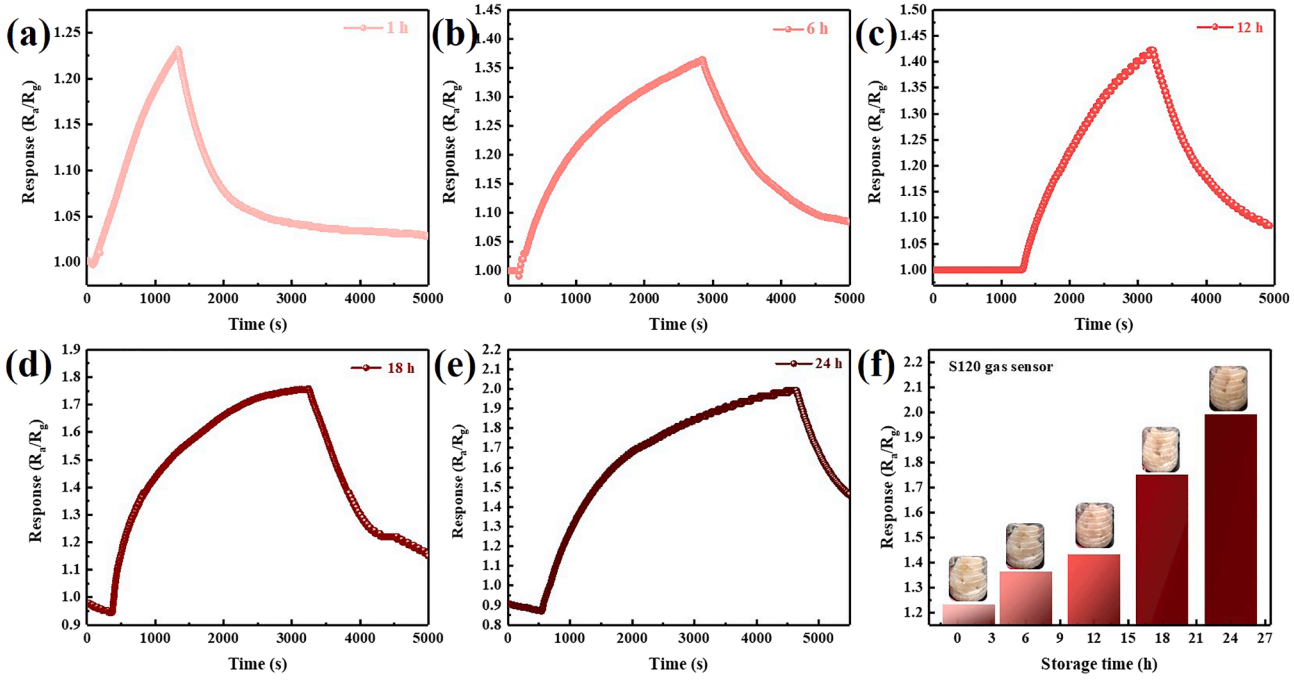

Fig. 6. (a-e) Responses of the S120 gas sensor to the odors from 25 g pangasius during different times (1, 6, 12, 18, 24 h). (f) Response values of S120 gas sensor and photographs of fish after storage for 24 h.

CRediT authorship contribution statement

Kaidi Wu: Conceptualization, Methodology, Investigation, Writing – original draft, Writing – review & editing. **Wentao Zhang:** Methodology, Investigation. **Zichen Zheng:** Methodology, Investigation. **Marc Debliquy:** Writing – review & editing. **Chao Zhang:** Supervision, Funding acquisition, Resources, Writing – review & editing.

Declaration of Competing Interest

The authors declare that they have no known competing financial interests or personal relationships that could have appeared to influence the work reported in this paper.

Acknowledgment

This work is supported by the National Natural Science Foundation of China under Grant No. 51872254, the Outstanding Youth Foundation of Jiangsu Province of China under Grant No. BK20211548, the National Key Research and Development Program of China under Grant No. 2017YFE0115900, the Jiangsu Postgraduate Research and Innovation Program under Grant No. KYCX21_3229 and the Excellent Doctoral Dissertation Fund of Yangzhou University (2021).

Appendix A. Supplementary data

Supplementary data to this article can be found online at https://doi.org/10.1016/j.apsusc.2022.152744.

References

[1] A. Mirzaei, S.S. Kim, H.W. Kim, Resistance-based H2S gas sensors using metal oxide nanostructures: A review of recent advances, J. Hazard. Mater. 357 (2018) 314–331, https://doi.org/10.1016/j.jhazmat.2018.06.015.
[2] M. Kaur, B.K. Dadhich, R. Singh, T. KailasaGanapathi, S. Bagwaiya, A. K. Bhattacharya, K.P. Debnath, S.C.G. Muthe, RF sputtered SnO2: NiO thin films as sub-ppm H2S sensor operable at room temperature, Sens. Actuators B Chem. 242 (2017) 389–403, https://doi.org/10.1016/j.snb.2016.11.054.
[3] M. Yang, X. Cheng, X. Zhang, W. Liu, C. Huang, Y. Xu, S. Gao, H. Zhao, L. Huo, Preparation of highly crystalline NiO meshed nanowalls via ammonia volatilization liquid deposition for H2S detection, J. Colloid Interface Sci. 540 (2019) 39–50, https://doi.org/10.1016/j.jcis.2018.12.106.
[4] G. Olafsdottir, P. Nesvadba, C. Di Natale, M. Careche, J. Oehlenschläger, S. V. Tryggvadóttir, R. Schubring, M. Kroeger, K. Heia, M. Esaiassen, A. Macagnano, B.M. Jørgensen, Multisensor for fish quality determination, Trends Food Sci. Technol. 15 (2004) 86–93, https://doi.org/10.1016/j.tifs.2003.08.006.
[5] S. Muthusamy, K. Rajalakshmi, D. Zhu, et al., A novel lysosome targeted fluorophore for H2S sensing: Enhancing the quantitative detection with successive reaction sites, Sens Actuators B Chem 320 (2020), 128433, https://doi.org/10.1016/j.snb.2020.128433.
[6] H. Shin, D.-H. Kim, W. Jung, J.-S. Jang, Y.H. Kim, Y. Lee, K. Chang, J. Lee, J. Park, K. Namkoong, I.-D. Kim, Surface activity-tuned metal oxide chemiresistor: Toward direct and quantitative halitosis diagnosis, ACS Nano. 15 (2021) 14207–14217, https://doi.org/10.1021/acsnano.1c01350.
[7] S.-J. Kim, S.-J. Choi, J.-S. Jang, N.-H. Kim, M. Hakim, H.L. Tuller, I.-D. Kim, Mesoporous WO3 nanofibers with protein-templated nanoscale catalysts for detection of trace Biomarkers in exhaled breath, ACS Nano. 10 (2016) 5891–5899, https://doi.org/10.1021/acsnano.6b01196.
[8] K. Wu, C. Zhang, Facile synthesis and ppb-level H2S sensing performance of hierarchical CuO microflowers assembled with nano-spindles, J. Mater. Sci. Mater. Electron. 31 (2020) 7937–7945, https://doi.org/10.1007/s10854-020-03332-8.
[9] P.L. Quang, N.D. Cuong, T.T. Hoa, H.T. Long, C.M. Hung, D.T.T. Le, N.V. Hieu, Simple post-synthesis of mesoporous p-type Co3O4 nanochains for enhanced H2S gas sensing performance, Sens. Actuators B Chem. 270 (2018) 158–166, https://doi.org/10.1016/j.snb.2018.05.026.
[10] D. Nagmani, A. Pravarthana, T.C. Tyagi, W. Jagadale, D.K. Prellier, Aswal, Highly sensitive and selective H2S gas sensor based on TiO2 thin films, Appl. Surf. Sci. 549 (2021), 149281, https://doi.org/10.1016/j.apsusc.2021.149281.
[11] S.M. Gupta, M. Tripathi, A review of TiO2 nanoparticles, Chin. Sci. Bull. 56 (2011) 1639, https://doi.org/10.1007/s11434-011-4476-1.
[12] E.K. Alenezy, Y.M. Sabri, A.E. Kandjani, D. Korcoban, et al., Low-temperature hydrogen sensor: Enhanced performance enabled through photoactive Pd-decorated TiO2 colloidal crystals, ACS Sens. 5 (2020) 3902–3914, https://doi.org/10.1021/acssensors.0c01387.
[13] V. Galstyan, A. Ponzoni, I. Kholmanov, M.M. Natile, E. Comini, S. Nematov, G. Sberveglieri, Investigation of reduced graphene oxide and a Nb-doped TiO2 nanotube hybrid structure To improve the gas-sensing response and selectivity, ACS Sens. 4 (2019) 2094–2100, https://doi.org/10.1021/acssensors.9b00772.
[14] A. Šutka, R. Eglitis, A. Kuzma, K. Smits, A. Zukuls, J.D. Prades, C. Fàbrega, Photodoping-inspired room-temperature gas sensing by anatase TiO2 quantum dots, ACS Appl. Nano Mater. 4 (2021) 2522–2527, https://doi.org/10.1021/acsanm.0c03089.
[15] S. Li, L. Xie, M. He, X. Hu, G. Luo, C. Chen, Z. Zhu, Metal-organic frameworks-derived bamboo-like CuO/In2O3 Heterostructure for high-performance H2S gas sensor with Low operating temperature, Sens. Actuators B Chem. 310 (2020), 127828, https://doi.org/10.1016/j.snb.2020.127828.
[16] M.-H. Kim, J.-S. Jang, W.-T. Koo, S.-J. Choi, S.-J. Kim, D.-H. Kim, I.-D. Kim, Bimodally porous WO3 microbelts functionalized with Pt catalysts for selective H2S sensors, ACS Appl. Mater. Interfaces. 10 (2018) 20643–20651, https://doi.org/10.1021/acsami.8b00588.
[17] X. Qiao, Y. Xu, K. Yang, J. Ma, C. Li, H. Wang, L. Jia, Mo doped BiVO4 gas sensor with high sensitivity and selectivity towards H2S, Chem. Eng. J. 395 (2020), 125144, https://doi.org/10.1016/j.cej.2020.125144.
[18] Z. Wu, Z. Li, H. Li, M. Sun, S. Han, C. Cai, W. Shen, Y. Fu, Ultrafast response/recovery and high selectivity of the H2S gas sensor based on α-Fe2O3 nano-ellipsoids from one-step hydrothermal synthesis, ACS Appl. Mater. Interfaces. 11 (2019) 12761–12769, https://doi.org/10.1021/acsami.8b22517.
[19] H. Liu, S. Xu, M. Li, G. Shao, H. Song, W. Zhang, W. Wei, M. He, L. Gao, H. Song, J. Tang, Chemiresistive gas sensors employing solution-processed metal oxide quantum dot films, Appl. Phys. Lett. 105 (2014), 163104, https://doi.org/10.1063/1.4900405.
[20] Y. Huan, K. Wu, C. Li, H. Liao, M. Debliquy, C. Zhang, Micro-nano structured functional coatings deposited by liquid plasma spraying, J. Adv. Ceram. 9 (2020) 517–534, https://doi.org/10.1007/s40145-020-0402-9.
[21] S. Cao, N. Sui, P. Zhang, T. Zhou, J. Tu, T. Zhang, TiO2 nanostructures with different crystal phases for sensitive acetone gas sensors, J. Colloid Interface Sci. 607 (2022) 357–366, https://doi.org/10.1016/j.jcis.2021.08.215.
[22] Y. Li, Y.L. Lu, K.D. Wu, D.Z. Zhang, M. Debliquy, C. Zhang, Microwave-assisted hydrothermal synthesis of copper oxide-based gas-sensitive nanostructures, Rare Met. 40 (2021) 1477–1493, https://doi.org/10.1007/s12598-020-01557-4.
[23] Y. Ding, I.S. Yang, Z. Li, X. Xia, W.I. Lee, S. Dai, D.W. Bahnemann, J.H. Pan, Nanoporous TiO2 spheres with tailored textural properties: Controllable synthesis, formation mechanism, and photochemical applications, Prog. Mater. Sci. 109 (2020), 100620, https://doi.org/10.1016/j.pmatsci.2019.100620.
[24] P.-X. Gao, Microwaves in nanoparticle synthesis. Fundamentals and spplications. Edited by Satoshi Horikoshi and Nick Serpone, Angew. Chem. Int. Ed. 53 (2014), https://doi.org/10.1002/anie.201404498, 7986–7986.
[25] H. Mahmood, M.A. Khan, B. Mohuddin, T. Iqbal, Solution-phase growth of tin oxide (SnO2) nanostructures: Structural, optical and photocatalytic properties, Mater. Sci. Eng. B. 258 (2020), 114568, https://doi.org/10.1016/j.mseb.2020.114568.
[26] H. Lin, C.P. Huang, W. Li, C. Ni, S.I. Shah, Y.-H. Tseng, Size dependency of nanocrystalline TiO2 on its optical property and photocatalytic reactivity exemplified by 2-chlorophenol, Appl. Catal. B Environ. 68 (2006) 1–11, https://doi.org/10.1016/j.apcatb.2006.07.018.
[27] C. Jiang, K.Y. Lee, C.M.A. Parlett, M.K. Bayazit, C.C. Lau, Q. Ruan, S.J.A. Moniz, A. F. Lee, J. Tang, Size-controlled TiO2 nanoparticles on porous hosts for enhanced photocatalytic hydrogen production, Appl. Catal. Gen. 521 (2016) 133–139, https://doi.org/10.1016/j.apcata.2015.12.004.
[28] M. Hou, J. Gao, L. Yang, S. Guo, T. Hu, Y. Li, Room temperature gas sensing under UV light irradiation for Ti3C2Tx MXene derived lamellar TiO2-C/g-C3N4 composites, Appl. Surf. Sci. 535 (2021), 147666, https://doi.org/10.1016/j.apsusc.2020.147666.
[29] T.M. David, K.I. Gnanasekar, P. Wilson, P. Sagayaraj, T. Mathews, Effect of Ni, Pd, and Pt nanoparticle dispersion on thick films of TiO2 nanotubes for hydrogen sensing: TEM and XPS studies, ACS Omega. 5 (2020) 11352–11360, https://doi.org/10.1021/acsomega.0c00292.
[30] J. Choi, Y.-J. Kim, S.-Y. Cho, K. Park, H. Kang, S.J. Kim, H.-T. Jung, In Situ Formation of multiple schottky barriers in a Ti3C2 MXene film and its application in highly sensitive gas sensors, Adv. Funct. Mater. 30 (2020) 2003998, https://doi.org/10.1002/adfm.202003998.
[31] Z. Wang, A. Ali Haidry, L. Xie, A. Zavabeti, Z. Li, W. Yin, R. Lontio Fomekong, B. Saruhan, Acetone sensing applications of Ag modified TiO2 porous nanoparticles synthesized via facile hydrothermal method, Appl. Surf. Sci. 533 (2020), 147383, https://doi.org/10.1016/j.apsusc.2020.147383.
[32] N. Mintcheva, P. Srinivasan, J.B.B. Rayappan, A.A. Kuchmizhak, S. Gurbatov, S. A. Kulinich, Room-temperature gas sensing of laser-modified anatase TiO2 decorated with Au nanoparticles, Appl. Surf. Sci. 507 (2020), 145169, https://doi.org/10.1016/j.apsusc.2019.145169.
[33] J. Zhang, C. Chen, H. Lu, D. Leng, G. Li, Y. Liu, Q. Liang, J. Gao, C. Wang, B. Zhu, Construction of anatase@rutile core@shell TiO2 nanosheets with controllable shell layer thicknesses for enhanced ethanol sensing, Sens. Actuators B Chem. 325 (2020), 128815, https://doi.org/10.1016/j.snb.2020.128815.
[34] C. Xu, J. Tamaki, N. Miura, N. Yamazoe, Grain size effects on gas sensitivity of porous SnO2-based elements, Sens. Actuators B Chem. 3 (1991) 147–155, https://doi.org/10.1016/0925-4005(91)80207-Z.
[35] D. Liu, Z. Tang, Z. Zhang, Visible light assisted room-temperature NO2 gas sensor based on hollow SnO2@SnS2 nanostructures, Sens. Actuators B Chem. 324 (2020), 128754, https://doi.org/10.1016/j.snb.2020.128754.
[36] K.-D. Wu, J.-Y. Xu, M. Debliquy, C. Zhang, Synthesis and NH3/TMA sensing properties of CuFe2O4 hollow microspheres at low working temperature, Rare Met. 40 (2020) 1768–1777, https://doi.org/10.1007/s12598-020-01609-9.

[37] S.W. Benson, III - Bond energies, J. Chem. Educ. 42 (1965) 502–518, https://doi.org/10.1021/ed042p502.
[38] J.A. Kerr, Bond dissociation energies by kinetic methods, Chem. Rev. 66 (1966) 465–500, https://doi.org/10.1021/cr60243a001.
[39] V. Galstyan, "Quantum dots: Perspectives in next-generation chemical gas sensors" - A review, Anal. Chim. Acta. 1152 (2021), 238192, https://doi.org/10.1016/j.aca.2020.12.067.
[40] M.S. Choi, A. Mirzaei, H.G. Na, et al., Facile and fast decoration of SnO2 nanowires with Pd embedded SnO2-x nanoparticles for selective NO2 gas sensing, Sens Actuators B Chem 340 (2021), 129984, https://doi.org/10.1016/j.snb.2021.129984.
[41] N.D. Chinh, C. Kim, D. Kim, UV-light-activated H2S gas sensing by a TiO2 nanoparticulate thin film at room temperature, J. Alloys Compd. 778 (2019) 247–255, https://doi.org/10.1016/j.jallcom.2018.11.153.
[42] X. Tong, W. Shen, X. Chen, et al., A fast response and recovery H2S gas sensor based on free-standing TiO2 nanotube array films prepared by one-step anodization method, Ceram Int 43 (2017) 14200–14209, https://doi.org/10.1016/j.ceramint.2017.07.165.
[43] X. Tong, W. Shen, X. Zhang, J.-P. Corriou, H. Xi, Synthesis and density functional theory study of free-standing Fe-doped TiO2 nanotube array film for H2S gas sensing properties at low temperature, J. Alloys Compd. 832 (2020), 155015, https://doi.org/10.1016/j.jallcom.2020.155015.
[44] S. Ma, J. Jia, Y. Tian, L. Cao, S. Shi, X. Li, X. Wang, Improved H2S sensing properties of Ag/TiO2 nanofibers, Ceram. Int. 42 (2016) 2041–2044, https://doi.org/10.1016/j.ceramint.2015.09.034.
[45] Z. Li, Y. Huang, S. Zhang, W. Chen, Z. Kuang, D. Ao, W. Liu, Y. Fu, A fast response & recovery H2S gas sensor based on α-Fe2O3 nanoparticles with ppb level detection limit, J. Hazard. Mater. 300 (2015) 167–174, https://doi.org/10.1016/j.jhazmat.2015.07.003.
[46] S. Yang, Z. Song, N. Gao, Z. Hu, L. Zhou, J. Liu, B. Zhang, G. Zhang, S. Jiang, H.-Y. Li, H. Liu, Near room temperature operable H2S sensors based on In2O3 colloidal quantum dots, Sens. Actuators B Chem. 286 (2019) 22–31, https://doi.org/10.1016/j.snb.2019.01.110.
[47] S.-K. Shen, X.-L. Cui, C.-Y. Guo, X. Dong, X.-F. Zhang, X.-L. Cheng, L.-H. Huo, Y.-M. Xu, Sensing mechanism of Ag/α-MoO3 nanobelts for H2S gas sensor, Rare Met. 40 (2021) 1545–1553, https://doi.org/10.1007/s12598-020-01647-3.
[48] A. Rothschild, Y. Komem, The effect of grain size on the sensitivity of nanocrystalline metal-oxide gas sensors, J. Appl. Phys. 95 (2004) 6374–6380, https://doi.org/10.1063/1.1728314.
[49] B. Lyson-Sypien, A. Czapla, M. Lubecka, P. Gwizdz, K. Schneider, K. Zakrzewska, K. Michalow, T. Graule, A. Reszka, M. Rekas, A. Lacz, M. Radecka, Nanopowders of chromium doped TiO2 for gas sensors, Sens. Actuators B Chem. 175 (2012) 163–172, https://doi.org/10.1016/j.snb.2012.02.051.
[50] Y. Xu, L. Zheng, C. Yang, W. Zheng, X. Liu, J. Zhang, Chemiresistive sensors based on core-shell ZnO@TiO2 nanorods designed by atomic layer deposition for n-butanol detection, Sens. Actuators B Chem. 310 (2020), 127846, https://doi.org/10.1016/j.snb.2020.127846.
[51] R.L. Wilson, C.E. Simion, C.S. Blackman, C.J. Carmalt, A. Stanoiu, F. Di Maggio, J. A. Covington, The effect of film thickness on the gas sensing properties of ultra-thin TiO2 Films deposited by atomic layer deposition, Sensors. 18 (2018) 735, https://doi.org/10.3390/s18030735.
[52] L. Li, P.A. Salvador, G.S. Rohrer, Photocatalysts with internal electric fields, Nanoscale. 6 (2014) 24–42, https://doi.org/10.1039/C3NR03998F.
[53] Z. Song, S. Xu, J. Liu, Z. Hu, N. Gao, J. Zhang, F. Yi, G. Zhang, S. Jiang, H. Liu, Enhanced catalytic activity of SnO2 quantum dot films employing atomic ligand-exchange strategy for fast response H2S gas sensors, Sens. Actuators B Chem. 271 (2018) 147–156, https://doi.org/10.1016/j.snb.2018.05.122.
[54] T.P. Mokoena, H.C. Swart, K.T. Hillie, Z.P. Tshabalala, M. Jozela, J. Tshilongo, D. E. Motaung, Enhanced propanol gas sensing performance of p-type NiO gas sensor induced by exceptionally large surface area and crystallinity, Appl. Surf. Sci. 571 (2022), 151121, https://doi.org/10.1016/j.apsusc.2021.151121.
[55] A. Katoch, G.-J. Sun, S.-W. Choi, J.-H. Byun, S.S. Kim, Competitive influence of grain size and crystallinity on gas sensing performances of ZnO nanofibers, Sens. Actuators B Chem. 185 (2013) 411–416, https://doi.org/10.1016/j.snb.2013.05.030.
[56] S. Das, S. Mojumder, D. Saha, M. Pal, Influence of major parameters on the sensing mechanism of semiconductor metal oxide based chemiresistive gas sensors: A review focused on personalized healthcare, Sens. Actuators B Chem. 352 (2022), 131066, https://doi.org/10.1016/j.snb.2021.131066.
[57] C. Zhang, et al., Preparation of ZnO1-x by peroxide thermal decomposition and its room temperature gas sensing properties, Rare Met. (2021), https://doi.org/10.1007/s12598-021-01840-y.
[58] C. Zhang, K. Wu, H. Liao, M. Debliquy, Room temperature WO3-Bi2WO6 sensors based on hierarchical microflowers for ppb-level H2S detection, Chem. Eng. J. 430 (2022), 132813, https://doi.org/10.1016/j.cej.2021.132813.